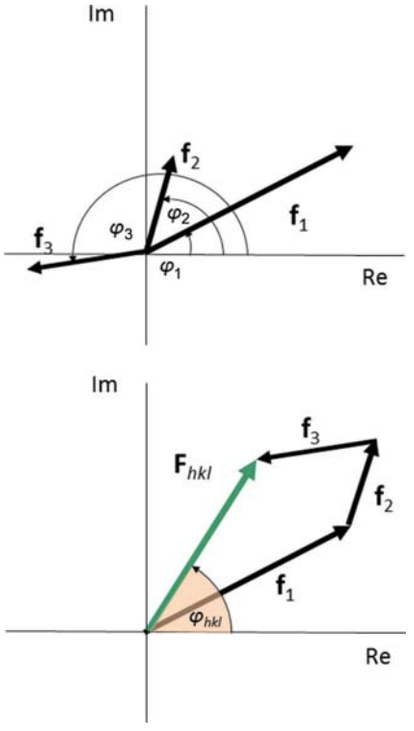

Figure 1.1.16
Graphical illustration of the summation of scattered wave amplitudes $\mathbf{f}_t$ in the complex plane, accounting for the phase shifts coming from the different positions of the atoms in the unit cell.

lattice points (directions of the Bragg peaks), and their intensities are multiplied by a factor, the crystallographic structure factor,

$$F_{hkl} = \sum_{t=1}^{m} f_t(h) \exp(2\pi i \mathbf{h} \cdot \mathbf{u}_t). \qquad (1.1.56)$$

If we write each term as a complex number denoted $\mathbf{f}_t$, we can represent this complex sum as a vector sum in the complex plane, as illustrated in Fig. 1.1.16, where the $\varphi_t = 2\pi \mathbf{h} \cdot \mathbf{u}_t$. The intensity of the Bragg peak depends only on the length of the $\mathbf{F}_{hkl}$, not its direction. However, its length depends on both the lengths *and the phases* of each contribution, which in turn depend on the positions of the atoms within the unit cell. This is the phase information that is 'lost' in a diffraction experiment. Given a structure, we can directly calculate all the Bragg-peak intensities (the 'forward problem'). However, given all the Bragg-peak intensities, we cannot directly calculate the structure (the 'inverse problem'). Structure determination uses the measured intensities and reconstructs the lost phase information using various iterative methods and algorithms.

In fact, the intensity of a Bragg reflection *hkl* is given by the squared absolute value of the structure-factor amplitude F_{hkl},

$$\left|F_{hkl}\right|^2 = \sum_{t,t'=1}^{m} f_t(h) f_{t'}^*(h) \exp\left(2\pi i \mathbf{h} \cdot (\mathbf{u}_t - \mathbf{u}_{t'})\right), \qquad (1.1.57)$$

where * indicates the complex conjugate. This analysis shows that the *positions* of the Bragg peaks determine the geometry of the periodic lattice (the size and shape of the unit cell, for example), but the *intensities* of the Bragg peaks are determined by the relative positions of atoms within the unit cell, scaled by their respective scattering power. To solve the internal structure of the structural motif within the unit cell, it is necessary to measure quantitatively the intensities of many Bragg peaks and use some kind of iterative procedure to move the atoms within the cell until the calculated structure factors self-consistently reproduce the intensities of all the measured Bragg peaks.

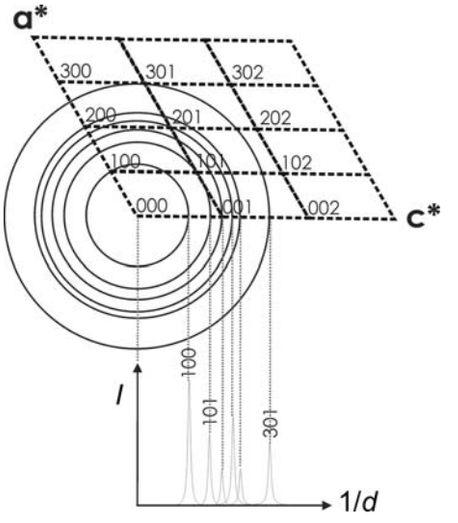

Figure 1.1.17
Schematic illustration of the projection of the reciprocal **a***c* plane (representing the three-dimensional reciprocal-lattice space) into the one-dimensional powder pattern.

The situation is not fundamentally different in a powder diffraction experiment from the single-crystal case, except that the Bragg peaks in three-dimensional reciprocal space are projected into one dimension, as shown in Fig. 1.1.17.

'Indexing' is the term used for deriving the lattice parameters from the positions of the Bragg peaks (see Chapter 3.4). Once the size and shape of the reciprocal lattice is determined, Miller indices can be assigned to each of the Bragg peaks in a one-dimensional powder pattern. If it is possible to extract the intensities of those peaks from the pattern, diffraction data from a powder can be used to reconstruct the three-dimensional structure in exactly the same way as is done with data from a single crystal. This process is known as structure solution from powder diffraction, and is often successful, although it is less well automated than structure solution from data from single crystals. As mentioned above, the main problem with powder data is a loss of information due to systematic and accidental peak overlap, but this can often be overcome.

There are various methods for extracting quantitative peak intensities from indexed powder patterns by computer fitting of profiles to the Bragg peaks at their known positions. Two of the most common are Pawley refinement (Pawley, 1981) and Le Bail refinement (Le Bail *et al.*, 1988), as discussed in Chapter 3.5.

In general, the intensities of the Bragg reflections must be corrected by the product K_{hkl} of various correction factors. Some common correction factors are given by

$$K_{hkl} = M_{hkl} \mathrm{Abs}_{hkl} \mathrm{Ext}_{hkl} \mathrm{LP}_{hkl} \mathrm{PO}_{hkl} \ldots, \qquad (1.1.58)$$

where M_{hkl} is the multiplicity, Abs_{hkl} is an absorption correction, Ext_{hkl} is an extinction correction, LP_{hkl} is the geometrical Lorentz–polarization correction and PO_{hkl} is a correction for preferred orientation (see Chapter 4.7).

If there is more than one crystalline phase present in the sample, and the structures of all the crystalline phases are known, then we can find a scale factor for each phase in the mixture which reproduces the data. This is then a way of determining the proportion of each phase in the sample. This is called quantitative phase analysis (see Chapter 3.9).

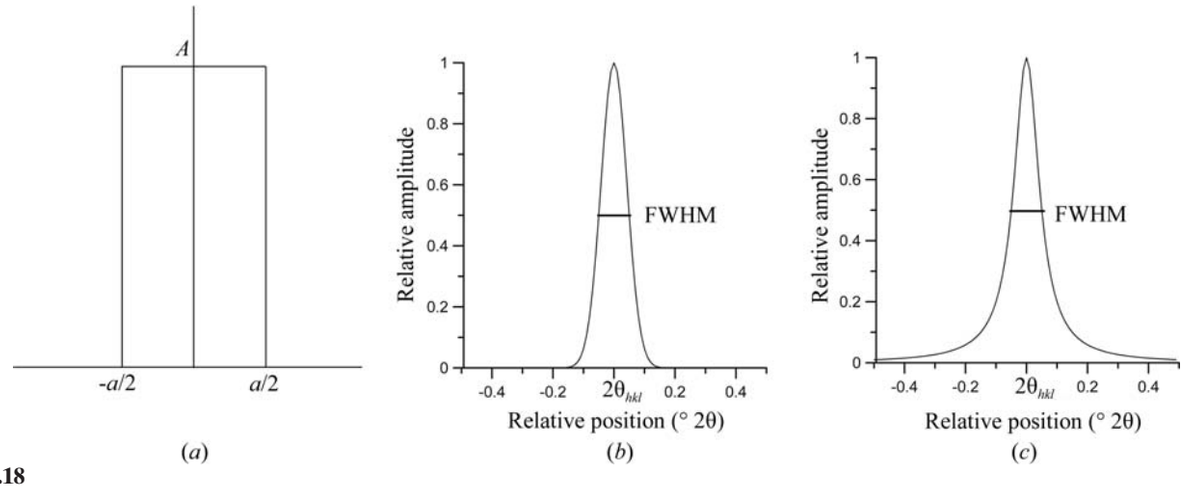

Figure 1.1.18
Normalized peak-shape functions. (*a*) The hat function, (*b*) the Gaussian function and (*c*) the Lorentzian function.

1.1.4. The peak profile

The peak profile refers to the shape of the measured Bragg peak. In the treatment above, the Bragg peaks from a perfect infinite crystal were delta functions and therefore infinitely narrow. In reality, the finite size of the crystal, the finite resolution of the measurement and defects in the material that result in inhomogeneous strains all broaden the delta function, giving it a finite width and some characteristic shape. When fitting a model to the measured diffraction pattern we should correctly account for these effects in order to obtain correct values for the Bragg-peak intensities. On the other hand, a careful study of the peak shapes yields important information about the size of the crystallites in the sample and defects that they contain. With recent improvements in instrumentation and computational data-analysis methods, this latter type of study has become more important and is having considerable scientific and technological impact.

The convolution theorem of the Fourier transform that was introduced in the derivation of the crystallographic structure factor above is also very useful in understanding the peak profile. In this case, the measured Bragg peak can be thought of as a delta function convoluted with a profile (Klug & Alexander, 1974). The profile of the Bragg reflection *hkl*, Φ_{hkl}, can be written as

$$\Phi_{hkl}(2\theta_i - 2\theta_{hkl}) = \mathrm{EP}(2\theta_i) \otimes \mathrm{IP}(2\theta_i) \otimes \mathrm{MS}(2\theta_i - 2\theta_{hkl}), \tag{1.1.59}$$

where $\mathrm{EP}(2\theta_i)$ is the emission profile of the X-ray source (tube or synchrotron), $\mathrm{IP}(2\theta_i)$ contains additional contributions to the profile from the instrument and $\mathrm{MS}(2\theta_i - 2\theta_{hkl})$ is the contribution from the microstructure of the sample. The symbol $\otimes$ denotes convolution.

The convolution of two functions $f(t)$ and $g(t)$ in real space is defined as

$$(f \otimes g)(t) = \int_{\tau=-\infty}^{\infty} f(\tau) g(t-\tau)\, \mathrm{d}\tau. \tag{1.1.60}$$

The convolution theorem tells us that the Fourier transform (FT) of two convoluted functions is the product of the Fourier transforms of those functions:

$$\mathrm{FT}(f \otimes g)(t) = \big(\mathrm{FT}(f)\big)\big(\mathrm{FT}(g)\big). \tag{1.1.61}$$

Normalization of the transform leads to scaling factors like 2π which have been omitted here for simplicity.

In practice, numerical integrations are almost always required, as many of the instrument aberration functions cannot be convoluted analytically. This convolution approach is the basis of the so-called fundamental-parameter (FP) approach (Cheary & Coelho, 1992) and has proven to be superior to other more empirical or phenomenological methods. The idea behind the FP approach is to build up the profile from first principles, exclusively using measurable physical quantities like slit widths, slit lengths, Soller-slit opening angles *etc*. The process of convolution from a fundamental-parameters perspective is an approximation whereby second- and higher-order effects are typically neglected for computational speed and simplicity. The instrumental profile is usually fully characterized by measuring a line-profile standard such as NIST SRM 660c LaB_6, which is expected to contain only small microstructural contributions, and comparing the calculated diffraction pattern to the measured one. Once the instrumental part of the profile is sufficiently well determined, it can be assumed that the remaining contributions to the 'real' profile are purely sample dependent (*e.g.* domain size, strain).

In general, it is desirable to keep the number of functions that are used to describe the peak profile to a minimum. Typical examples of mathematical functions which are convoluted to form the profile of a Bragg reflection include:

(*a*) the hat function H (*e.g.* for all kinds of rectangular slits),

$$H(2\theta - 2\theta_{hkl}) = \begin{cases} A \text{ for } -a/2 < (2\theta - 2\theta_{hkl}) < a/2, \\ 0 \text{ for } (2\theta - 2\theta_{hkl}) \le -a/2 \\ \quad \text{and } (2\theta - 2\theta_{hkl}) \ge -a/2 \end{cases} \tag{1.1.62}$$

(Fig. 1.1.18*a*);

(*b*) the normalized Gaussian G (*e.g.* for microstrain broadening),

$$G(2\theta - 2\theta_{hkl}) = \left(\frac{2\sqrt{\ln(2)/\pi}}{\mathrm{FWHM}}\right) \exp\left(\frac{-4\ln(2)(2\theta - 2\theta_{hkl})^2}{\mathrm{FWHM}^2}\right), \tag{1.1.63}$$

(Fig. 1.1.18*b*), where FWHM denotes the full width at half maximum of the Gaussian function in ° 2θ; and

(*c*) the Lorentzian function L (*e.g.* for the emission profile),

$$L(2\theta - 2\theta_{hkl}) = \frac{1}{2\pi}\left(\frac{\mathrm{FWHM}}{(2\theta - 2\theta_{hkl}) + \mathrm{FWHM}^2/4}\right), \tag{1.1.64}$$

(Fig. 1.1.18*c*).

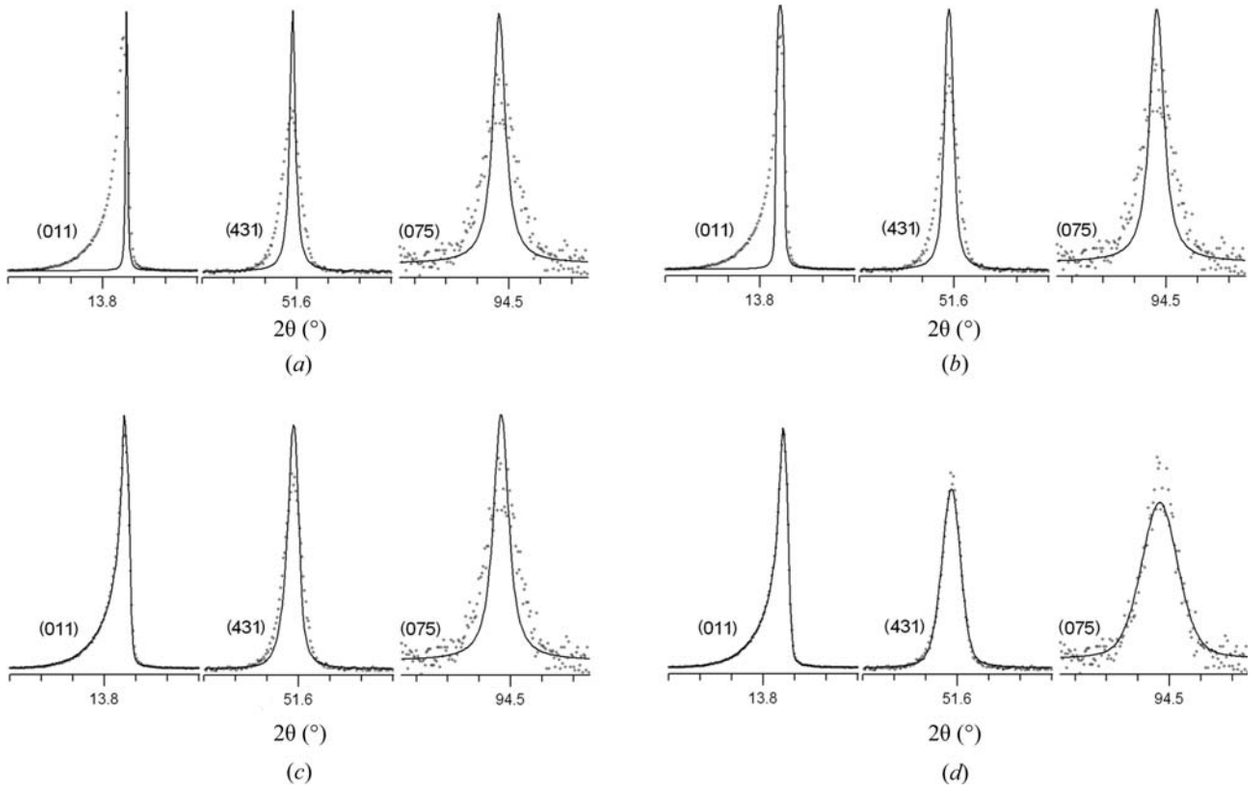

Figure 1.1.19
Peak fits of three selected reflections for an LaB_6 standard measured with Mo $K\alpha_1$ radiation ($\lambda = 0.7093$ Å) from a Ge(220) monochromator in Debye–Scherrer geometry using the fundamental-parameter approach. (*a*) A pure Lorentzian emission profile with a half width of 0.2695 mÅ is applied, refining the peak position and intensity only; (*b*) additionally, a hat shape function of the receiving slit in the equatorial plane with a width of 0.1 mm has been convoluted into the profile; (*c*) additionally, an axial convolution with filament-, sample- and receiving-slit lengths of 8 mm each and a secondary Soller slit with an opening angle of 2.5° has been convoluted into the profile; (*d*) additionally a small contribution of Gaussian broadening coming from the position-sensitive detector is convoluted into the profile. [From Mittemeijer & Welzel (2012). Copyright Wiley-VCH Verlag GmbH & Co. KGaA. Reproduced with permission.]

These functions can be convoluted sequentially as needed, first with the delta-function Bragg peak, and subsequently with the existing profile from the previous convolutions, each time resulting in a new profile that can become quite complex (Fig. 1.1.19). It is often the case that for a particular resolution effect the angular dependence of the profile function is known from the geometry of the measurement, and the convolution function for each peak is determined with only a very small number of parameters.

1.1.4.1. *Sample contributions to the peak profile*

Features of the sample that affect the peak profile include crystallite domain size and shape, dislocations, disclinations, twin and stacking faults, antiphase domains, microstrains, grain surface relaxations, and compositional fluctuations. Here we reproduce some basic results as examples; they also illustrate some fundamental aspects of diffraction from real crystals.

1.1.4.1.1. *Crystallite size*

The starting point for the analysis of finite size effects is the Laue equation, equation (1.1.39), which is reproduced here for a one-dimensional crystal:

$$A(h) = \sum_{j=0}^{n} \exp(2\pi i a j h). \tag{1.1.65}$$

When we were deriving the Bragg equation from the Laue equation we assumed an infinite crystal, and the sum taken to infinity resulted in delta functions at the reciprocal-lattice points. Now we want to consider a finite crystal with n unit cells. There is an analytic form for this sum which, using Euler's identity, is given by

$$\begin{aligned} A(h) &= \frac{\exp\left(2\pi i(n+1)ah\right) - 1}{\exp(2\pi i a h) - 1} \\ &= \frac{\exp\left(i\pi(n+1)ah\right)}{\exp(i\pi a h)} \frac{\exp\left(i\pi(n+1)ah\right) - \exp\left(-i\pi(n+1)ah\right)}{\exp(i\pi a h) - \exp(-i\pi a h)} \\ &= \exp(i\pi n a h) \frac{\sin\left(\pi(n+1)ah\right)}{\sin(\pi a h)}. \end{aligned} \tag{1.1.66}$$

The intensity is obtained by taking the modulus squared of this complex function, resulting in

$$I(h) = \frac{\sin^2\left(\pi(n+1)ah\right)}{\sin^2(\pi a h)}. \tag{1.1.67}$$

This function has sharp maxima when $h = \nu(1/a)$, where ν is an integer. This large central maximum falls off with a width proportional to $1/n^2$ with oscillating tails of intensity where the frequency of the oscillations increases with increasing n. This is illustrated in Fig. 1.1.20 for two different values of n but the same value of a.

In general, the Fourier transforms of periodic patterns become sharper with increasing number of unit cells. The expression $\sin(\pi(n+1)ah)/\sin(\pi a h)$ is also called the geometric factor of the structure amplitude.

This size broadening is often modelled in practice by using an equation due to Scherrer. We now reproduce the simple deri-

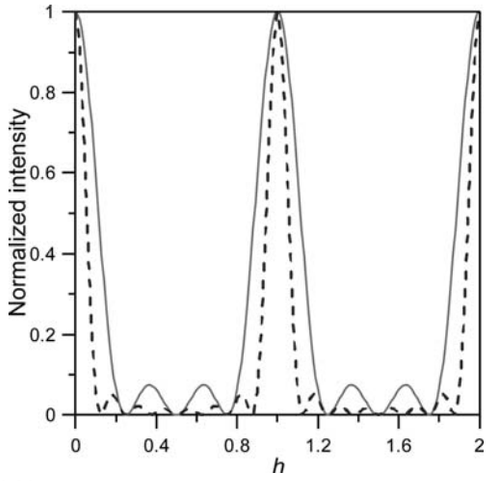

Figure 1.1.20
Normalized intensity from a finite lattice with $n = 3$ (solid curve) and $n = 8$ (dashed line), demonstrating the sharpening of peaks with increasing number of unit cells n. The normalization was done such that the peaks have the same peak maximum rather than the same integrated intensity for a clearer comparison of the relative peak widths.

vation of the Scherrer equation following Klug & Alexander (1974).

Fig. 1.1.21 shows the path-length difference *versus* the depth of the lattice plane. When the angle between the incoming beam and the lattice plane θ is different by an amount ε from the Bragg condition, it is always possible to find a lattice plane inside an infinite crystal where the extra path is $\Delta = \lambda(n + \frac{1}{2})$ for n integer, producing destructive interference. For a thick crystal this is true for arbitrarily small ε, which explains the sharp Bragg reflections. In the case of a crystal with finite dimensions, for small ε the plane for which $\Delta = \lambda(n + \frac{1}{2})$ holds will not be reached, thus leading to an intensity distribution over some small angular range. We can use this idea to estimate the broadening of a Bragg reflection due to size effects.

The thickness of a crystallite in the direction perpendicular to p planes of separation d_{hkl} (Fig. 1.1.21) is

$$L_{hkl} = p d_{hkl}. \tag{1.1.68}$$

The additional beam path between consecutive lattice planes at the angle $\theta + \varepsilon$ is

$$\begin{aligned}\Delta &= 2d\sin(\theta + \varepsilon)\\ &= 2d(\sin\theta\cos\varepsilon + \cos\theta\sin\varepsilon)\\ &= n\lambda\cos\varepsilon + 2d\sin\varepsilon\cos\theta\\ &\simeq n\lambda + 2d\sin\varepsilon\cos\theta.\end{aligned} \tag{1.1.69}$$

The corresponding phase difference is then

$$\delta\varphi = 2\pi\frac{\Delta}{\lambda} = 2\pi n + \frac{4\pi}{\lambda}\varepsilon d\cos\theta = \frac{4\pi\varepsilon d\cos\theta}{\lambda} \tag{1.1.70}$$

and the phase difference between the top and the bottom layer (layer p) is then

$$p\delta\varphi = p\frac{4\pi\varepsilon d\cos\theta}{\lambda} = \frac{4\pi L_{hkl}\varepsilon\cos\theta}{\lambda}. \tag{1.1.71}$$

Rearranging equation (1.1.71) leads to

$$\varepsilon = \frac{\lambda\delta\varphi}{4\pi L_{hkl}\cos\theta}, \tag{1.1.72}$$

which gives an expression for the misalignment angle in terms of the crystallite size L_{hkl} and the phase difference $\delta\varphi$ between the reflections originating from the top plane and the bottom plane. Clearly, the scattered intensity is at a maximum for $\delta\varphi = 0$ ($\varepsilon = 0$). With increasing ε the intensity decreases, giving rise to a peak of finite width. Perfect cancellation of the waves from the top and bottom planes occurs for a phase difference of $\delta\varphi = \pm\pi$, at which point $\varepsilon = \pm\lambda/(4L_{hkl}\cos\theta)$. On a 2θ scale, the measured angular width between these points is

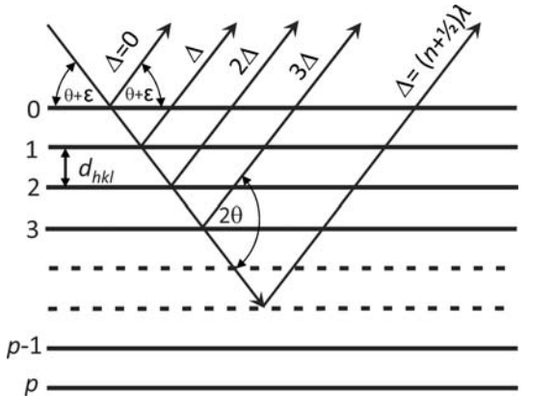

Figure 1.1.21
Path-length difference of the scattered ray *versus* the depth of the lattice plane in the crystal. [Reproduced from Dinnebier & Billinge (2008) with permission from the Royal Society of Chemistry.]

$$\beta_{hkl} = 4\varepsilon = \frac{\lambda}{L_{hkl}\cos\theta}, \tag{1.1.73}$$

giving us some measure of the peak width in radians that results from the finite particle size. A full treatment taking into account the correct form for the intensity distribution gives

$$\beta_{hkl} = \frac{K\lambda}{L_{hkl}\cos\theta}, \tag{1.1.74}$$

with a scale factor of $K = 0.89$ for perfect spheres. In general K depends on the shape of the grains (*e.g.* K is 0.94 for cube-shaped grains), but it is always close to unity. This equation is not valid for crystallites[3] that are too large or too small. In the case of large crystallites the peak width is governed by the coherence of the incident beam and not by particle size. For nanometre-sized crystallites, Bragg's law fails and the Debye equation needs to be used instead. The Debye equation (see Section 1.1.5.3) gives the scattering from an isotropically scattering sample such as a glass, liquid or powder, and does not presume that the sample is periodic.

1.1.4.1.2. *Microstrain*

Several important relationships in crystallography, including the effect of strain and microstrain on Bragg peaks, follow directly from a derivative of the Bragg equation (1.1.3). First we rewrite Bragg's law making the d-spacing the subject of the equation:

$$d = \frac{n\lambda}{2\sin\theta}. \tag{1.1.75}$$

The uncertainty of the measured lattice spacing is given by the total derivative dd,

$$\mathrm{d}d = \frac{\partial d}{\partial\theta}\mathrm{d}\theta + \frac{\partial d}{\partial\lambda}\mathrm{d}\lambda, \tag{1.1.76}$$

[3] Strictly speaking, the term crystallite size here refers to the dimension of a coherently scattering domain. Only in a perfect crystal is this the grain size.

Table 1.1.1
Types of scattering from a sample

Type of scattering	Coherent	Incoherent
Elastic	Bragg scattering Magnetic Bragg scattering Bragg scattering from ferroelectric/magnetic order Diffuse scattering from static defects Diffuse signal from small nanoparticles (<10 nm) Scattering from amorphous material (except excitations) Multiple scattering (coherent)	Laue monotonic diffuse scattering Neutron incoherent scattering Multiple scattering (incoherent)
Inelastic	Thermal diffuse scattering Spin-wave scattering Paraelectric/paramagnetic scattering Scattering from liquids	Compton scattering Fluorescence Incoherent scattering from hydrogen

leading to

$$\mathrm{d}d = -\frac{n\lambda}{2\sin\theta}\frac{\cos\theta}{\sin\theta}\mathrm{d}\theta + \frac{n}{2\sin\theta}\mathrm{d}\lambda \qquad (1.1.77)$$

and finally

$$\frac{\mathrm{d}d}{d} = -\frac{\mathrm{d}\theta}{\tan\theta} + \frac{\mathrm{d}\lambda}{\lambda}. \qquad (1.1.78)$$

When a crystal is strained, the d-spacings vary. A *macroscopic* strain changes the interplanar spacing by Δd_{hkl}, giving rise to a shift of $\Delta\theta$ in the *average* position of the diffraction peak. On the other hand, *microscopic* strains result in a distribution of d-spacings of width δd_{hkl}, which has the effect of *broadening* the diffraction peak by $\delta\theta$. Equation (1.1.78) gives an expression for the amount of Bragg-peak broadening that occurs for a given δd_{hkl}.

1.1.5. The background

1.1.5.1. *Information content in the background*

As discussed above, the elastic scattering from a crystalline powder consists of sharp rings, or peaks, of scattering at the 2θ angles where the Bragg or von Laue laws are satisfied. In general these sharp peaks sit on top of a 'background' which is broad and somewhat featureless. There are two components to this background, illustrated in Fig. 1.1.1: extraneous counts in the detector from things other than the sample, and non-Bragg scattering from the sample itself. The former are rarely of interest scientifically and the objective of a good experimental design is to minimize them as far as possible, or explicitly measure and subtract them, and then account well in any model or data interpretation for the part that cannot be eliminated from the measurement. Historically, the diffuse-scattering signals from the sample itself were also considered to be an inconvenience to be minimized and removed, and indeed in many cases this is still the best course of action (for example, sample fluorescence can be eliminated by choosing to work at an X-ray energy that lies below the absorption edge of a constituent atom). However, the diffuse 'background' from the sample can contain crucial information about defects, disorder and nanoscale order in the sample, and increasingly we are interested in studying it in order to understand the properties of the material that is under investigation. In some cases, such as glasses, liquids and samples of small nanoparticles, there is no Bragg scattering at all and only a diffuse scattering signal (see Chapter 5.6).

All the intensity scattered by the sample can be categorized as either coherent or incoherent and as elastic or inelastic, which are defined as follows. The coherency of the signal derives from whether or not the scattered waves interfere with each other constructively, and the resulting intensities are different in each case. For coherent scattering, the waves contributing to the signal are all summed first, before the wave amplitude is squared, to find the intensity distribution, which is the modulus squared of the resulting wave. For incoherent waves, one simply squares the amplitude of each wave to get its intensity and sums these together to get the total intensity. Switching to a consideration of the elasticity of the scattering, we define the scattering as elastic if the incident and scattered waves have the same energy, in which case no energy was exchanged during the scattering process between the incident wave and the sample, and inelastic scattering as the opposite. Inelastic scattering may result in a gain or a loss of energy of the scattered particle depending on the nature of the scattering, which results in a change in the wavelength of the scattered particle. There are also some non-scattering processes that can take place, such as absorption and fluorescence, but emissions resulting from these processes can also be categorized by whether or not they are coherent and elastic. It should be noted that the total energy of the system must be conserved during the scattering process, and so when a scattered wave gains or loses energy it exchanges it with the sample. This is used as a way of probing excitations in a material. Table 1.1.1 summarizes many of the types of diffuse scattering coming from a sample and categorizes them by their coherency and elasticity.

1.1.5.2. *Background from extraneous sources*

The most commonly observed extraneous, or parasitic, scattering is from the sample container (such as a capillary) that holds the sample during the measurement. Another large contribution may come from air scattering, which originates principally from scattering of the direct beam by molecules in the air in the beam path, both before and after the sample. Air-scattering effects can be minimized by enclosing as much of the beam path as possible in a tube which may be evacuated or where the air is replaced by a weakly scattering gas (such as He in the case of X-rays). Air scattering that is detected by the detector can also be reduced by careful collimation of the beams and then shielding the detector from detecting radiation that does not originate from the sample position. Collimating the incident beam is straightforward and results in a big reduction in air scattering. For point detectors it is also straightforward to collimate the scattered beam, but the modern trend towards using linear and area detectors makes this more difficult. There is sometimes a trade-off between collimating the scattered beam to reduce background and having uniform backgrounds that do not vary with angle because of